Modular microtissues for the regeneration of functional bone in large defects

Ramkumar T. Annamalai [a, 1], Xiaowei Hong [a], Nicholas Schott [a], Gopinath Tiruchinapally [a]

Benjamin Levi [b] and Jan P. Stegemann [a, 1]

[a] Department of Biomedical Engineering, [b] Department of Surgery

University of Michigan, Ann Arbor

[1]Corresponding Authors: Jan P. Stegemann

Department of Biomedical Engineering

University of Michigan

1101 Beal Ave.

Ann Arbor, MI 48109

Tel: 734-764-8313

Fax: 734-647-4834

Email: jpsteg@umich.edu (JPS), ramta@umich.edu (RTA)

Abstract: (<250 Words): Clinical bone healing impairment caused by altered biological or mechanical environment after bone fracture requires therapeutic interventions to avert delayed union or nonunion. Although cancellous bone grafting has its merits, they often necessitate revision surgeries and may not be useful for unopen defects with bone loss. Cell-based tissue engineering strategies have shown remarkable promise; however, most scaffold-based approaches involve invasive surgery for implantation. We have developed a minimally-invasive strategy that harnesses biomaterials to create modular microtissues containing autologous adipose-derived mesenchymal stromal cells (MSC). In the present study, chitosan-collagen based microtissues were designed to provide a suitable extracellular environment for osteogenic cells and were characterized by bone formation both in-vitro and in-vivo. In vitro characterization of cell-laden microtissues in suspension culture indicated robust osteogenesis of MSC under osteogenic conditions. In vivo analysis of microtissues in murine critical-sized calvarial defect showed that cells are necessary for bridging the defect while acellular microtissues can only form mineralized bone in apposition to the native bone. We also found that the osteogenically primed MSC can form mature collagenous lamellar and woven bone while the unprimed MSC are limited to creating osteoid-like structures embedded in fibrous connective tissues. Our modular microtissue strategy certainly helped to vascularize the constructs regardless of the cell presence and its phenotype. Embedding the microtissues in a fibrin carrier gel helped to contain the microtissues within the defect while conforming to the shape of the defect. The non-invasive delivery of microtissues was also demonstrated by injecting microtissues though a 23-gauge needle into critical-sized defect guided by non-invasive ultrasound imaging. Together, these microtissues can be used to augment the differentiated function of MSC and to provide a suitable extracellular environment to promote bone repair and integration and may have utility in clinical bone regeneration strategies.

Introduction:

Bone tissue has the regenerative capacity to repair itself, but the healing process in complex fractures and large bone defects that needs bridging fails in many cases. Loss of native vasculature and infection of the callus can further mitigate the regeneration process resulting in various pathologies including non-union. Impaired healing after bone fracture often requires therapeutic intervention to avert delayed- or non-union. Traditional bone grafting has proven to be a useful therapy but requires invasive surgeries. The autologous grafts are limited in supply and can cause donor-site morbidity and the associated risk of infection, hematoma, and pain [1]. Moreover, they are not suitable for 10-30% of patients due to difficulty in conforming the graft to the shape of the defect [2]. Further, shape-conforming constructs can yield superior results in case of procedures involving core decompression, cyst removal, and craniofacial surgeries. Allogeneic decellularized grafts and synthetic ceramic substitutes, on the other hand, are biologically inferior compared to viable bone grafts due to the lack of cellular components. Although processes such as irradiation and lyophilization can reduce the risk of disease transmission from an allogeneic graft, they eliminate cellular components resulting in reduced osteoinductivity [3] and revascularization resulting in higher bone resorption [4]. An ideal bone scaffold/substitute should exhibit osteoconductive, osteoinductive, and osteogenic properties and promote neovascularization [3]. The material properties of the scaffold could be optimized to augment osteoconduction, while cells are necessary for osteoinduction. Adult stem-cells are long known for their osteogenic potential, nevertheless only limited success has been achieved in translating to the clinic [5]. Studies show bone formation in apposition to grafted mesenchymal stromal cells (MSC) although not enough to bridge large defects [6]. Guiding stem cell phenotype after transplantation is an intense field of

research and combining biomaterial with adult stem cells have a significant potential to treat orthopedic bone defects.

Cell- and material-based strategies have shown promise to fulfill clinical demand [6], yet most approaches involve pre-formed scaffolds that require invasive surgery for implantation. An injectable scaffold would be more appealing to a wide range of defects and also can minimize complications due to surgery [7]. Injectable constructs not only offer minimally invasive delivery, which reduces infection and recovery time but also can conform to irregularly-shaped defects more readily. In case of unopened fractures with bone loss and craniofacial procedures, initially, injectable constructs are highly favored. For fabricating an injectable material-based construct, several parameters including mechanical properties, biocompatibility, degradation and gelation kinetics should be considered. Traditional approaches involve injecting cell-laden hydrogels that can be physically or chemically cross-linked in-situ. Although physically crosslinked hydrogels avoid exposing cells and proteins to harsh chemicals, they usually possess poor mechanical properties and thus may not suitable for orthopedic applications [8]. Chemically cross-linked hydrogels show enhanced mechanical features with the ability to engineer desirable degradation rates specifically but may exhibit cytotoxicity [7]. An ideal approach would be to develop a scalable method using microscale constructs or microtissues that integrate ECM architecture and stiffness while retaining their injectability. The modular microtissues should allow attachment, proliferation, and remodeling of cells before injecting them in-vivo. Such an approach would accelerate the wound healing process and hence ideal for orthopedic applications.

Bone is made up of hierarchical structures and mainly composed of collagen, glycosaminoglycans (GAG) and hydroxyapatite (HA) [9]. Collagen is the organic component of bone which possesses motifs for cell adhesion and subsequent cell response [10]. To mimic the

biomolecular and structural properties of bone ECM, collagen type I (hereafter referred to as collagen) is often combined with other biomaterials such as chitosan [11] and bioceramics [12, 13]. Chitosan is a natural biopolymer comprised of N-acetylglucosamine and glucosamine units which structurally and compositionally resembles glycosaminoglycans (GAG) [9] but with enhanced mechanical properties and osteoconductivity [14]. Therefore, combining chitosan and collagen along with HA nanoparticles will create a bone instructive and permissive matrix which mimics the organic and inorganic components of the natural bone. Based on this strategy, we have developed a minimally-invasive approach that harnesses chitosan-collagen-HA composite to create modular microtissues containing adipose-derived mesenchymal stromal cells (MSC), which can be injected as a slurry or paste to fill bone defects conformally.

2. Materials and Methods:

2.1 Cells and Biopolymers

Adipose mesenchymal stromal cells (MSC) were harvested by digesting inguinal fat pads from 6-8 week old transgenic C57BL/6 ROSA$^{mT/mG}$ (The Jackson Labs, Bar Harbor, ME) mice that express cell membrane-localized tdTomato (mT) fluorescence expression in all cells/tissues. The digestion solution comprised of 0.1 wt% collagenase in calcium and magnesium free phosphate buffered saline (PBS; Invitrogen). The harvested single cell suspension was filtered through a 70 μm cell strainer (Corning), suspended in Dulbecco's Modified Eagle's Medium (DMEM, Invitrogen) supplemented with 10% qualified FBS and 1% penicillin and streptomycin (Invitrogen) and cultured in tissue culture dishes. After 2-3 days of culture, adherent MSC were detached using TrypLE Express reagent (Invitrogen) and culture-expanded until passage 6 for use

in experiments. Standard osteogenic supplements (OST) were added to the respective expansion media for differentiating MSC.

The biopolymers used to make osteogenic microtissues were chitosan (Protosan UP B 90/500, Novamatrix, Philadelphia, PA) and type I collagen (MP Biomedicals Inc., Santa Ana, CA). Chitosan stock solution was made through a two-step process. First 0.25 g of chitosan flakes were suspended in 25 ml of water and autoclaved at 121ºC for 30 min. Then 30 µL of Glacial Acetic Acid (17.4 M) was added to the cooled suspension under sterile condition. The resulting solution (1 wt% chitosan in 0.02 N acetic acid) was stirred for seven days at 4ºC. The solution was then centrifuged at 10000 g to remove undissolved particles and used for making microtissues. Collagen stock solution was prepared by dissolving 250 mg of lyophilized collagen in 62.5 ml of sterile-filtered 0.02 N Acetic Acid. The resulting solution (0.4 wt% collagen in 0.02 N acetic acid) was stirred at 100-200 rpm for 7 days at 4ºC. The fully dissolved collagen solution was stored at 4ºC until microtissue fabrication.

2.2 Microtissue Fabrication and suspension-cultures

Chitosan/Collagen (CHI-COL) microtissues were fabricated using water-in-oil emulsification method (Schematically shown in **Fig. 1A)** modified from the previously described procedure [15, 16]. Briefly, cells were suspended in a hydrogel mixture made up of chitosan, collagen, β-glycerophosphate (58 wt% in water, Sigma, St.Louis, MO), and glyoxal (68.9 mM in water, Sigma). All stock solutions were kept on ice prior to making the microtissue. For each 5 ml of the hydrogel mixture, 2.5 ml of the collagen stock (0.4 wt% in 0.02 N acetic acid), 1.25 ml of chitosan stock (1 wt% chitosan in 0.02 N acetic acid), 0.6 ml of β-glycerophosphate (58 wt% in water) and 60 µL of glyoxal (68.9 mM in water) was added and mixed thoroughly. Finally, 0.6 ml of cell suspension was added to the neutralized mixture and mixed thoroughly by gentle vortex. To

enhance the osteogenic potential of the microtissues, HA nanoparticles (0.1 to 2 wt%) can be added to the mixture. Before adding to the mixture, the HA stock solution (300 mg/mL of PBS) is deflocculated by sonication. The cell-hydrogel mix was then dispensed dropwise to a stirred polydimethylsiloxane (PDMS, Clearco Products, Willow Grove, PA) bath kept in ice. The mixture was stirred by a dual radial-blade impeller at 800 rpm for 5 minutes to disperse the hydrogel composite into a fine emulsion in the PDMS. After 5 min, the temperature of the bath was increased to 37ºC stirred for an additional 30 minutes to promote gelation of the microtissue droplets. The emulsion was centrifuged at 200 g for 5 min to separate the microspheres. The PDMS supernatant was removed without disturbing the pellet, which was then washed twice with complete culture media and collected by centrifugation at 150 g for 5 min. The microtissues were equilibrated in 5 ml of complete culture media to remove unbound β-glycerophosphate. The microtissue were then culture in vented tissue culture tubes in suspension culture inside a standard CO_2 incubator at 37ºC.

The morphology, sphericity, and size distribution of the microtissues were analyzed from confocal stacks (Nikon A1 Confocal Microscope). ImageJ software (National Institutes of Health) was used to determine the size distribution and sphericity of the microtissues. Imaris software (Bitplane, Belfast, UK) was used for generating a 3D projection of the confocal stacks.

2.3 Mouse calvarial defect and implantation

All animal procedures were performed in compliance with the Guide for the Care and Use of Laboratory Animals at the University of Michigan and approved by the Chancellor's Animal Research Committee. All live animal surgical procedures were performed under 3-5% isoflurane/oxygen anesthesia. Immediately after induction, buprenorphine (0.05-0.1 µg/g body weight) and Xylazine (1.5 mg/kg) were administered for analgesia before the first surgical incision.

To prevent corneal dryness, a bland ophthalmic ointment was applied during surgery. Sterile pharmacy grade saline was also administered (0.02 mL/g body weight) subcutaneously, to prevent dehydration. The calvarial defect was done as previously described [17]. Briefly, after cleaning the surgical site with Betadine, a 1.5-2 cm incision was made just off the sagittal midline in order to expose the right parietal bone. The periosteum enveloping the skull (pericranium) was removed using a sterile cotton swab. Using a diamond-coated trephine bit and copious saline irrigation, unilateral 4 mm full-thickness critical-sized calvarial defect was created in the non-suture associated right parietal bone, taking care to avoid dural injury. After squirting the microtissue construct, the skin was sutured with 6-0 vicryl suture, and the animals were monitored as per the established post-operative animal care protocols. Animals were kept under warm pads during recovery and observed for 6 hours before being returned to the animal housing facility. Animals were monitored twice daily for three days and weekly after that to ensure postoperative recovery. Buprenorphine was administered every 12 hours for three days postoperatively.

2.4 In vivo imaging and analysis

In vivo bone formation was assessed with longitudinal micro-computed tomography (micro-CT) scans for 12 weeks. Micro-CT was performed, using a high-resolution SkyScan 1176 (Bruker, Billerica, MA) small animal imaging system up to 15 weeks. Images were reconstructed, and bone volume formation was analyzed using a MicroView software (GE Healthcare, London, Canada). Quantification was performed by selecting for new, calcified bone with a Hounsfield radiodensity of 1250 or higher based on Misch bone density classification [18]. Every mouse was scanned with a CT-phantom which included hydroxyapatite, water, and air for calibration.

To track the red fluorescent tdTomato (mT) from exogenously implanted MSC, the IVIS® Spectrum (PerkinElmer, Shelton, CT) in vivo imaging system and confocal microscope (Nikon

A1) was used. At week 12 the animals were sacrificed by CO_2 asphyxiation and cervical dislocation and imaged immediately after removing the skin to eliminate auto-fluorescence. The animal calvaria were placed in the imaging system and imaged for 2 sec at small binning. The fluorescence at the calvarial injury site was quantified using Living Image 3.2 (PerkinElmer). The calvarial were then fixed in buffered alcoholic formalin solution (Z-Fix, Anatech) and stained for DAPI (Invitrogen). After rinsing twice in 10 mM PBS, samples were resuspended in fresh PBS and images were captured using a confocal microscope (Nikon A1).

2.5 NMR Analysis

Nuclear magnetic resonance (NMR) spectroscopy was employed to study protein conformation, and modifications as previously described [19]. Briefly, collagen-chitosan microtissue samples were collected, washed in PBS, dialyzed (8 kDa MWCO) against DI water for 48 hours at 4°C and lyophilized to obtain dry samples. Then 2 mg of each sample was dissolved in deuterated water (D_2O, 0.5 mL) containing 0.5% CD_3COOD and dissolved at room temperature for 4 hours before analysis. ^1H NMR spectra in D_2O were recorded on 700 MHz Varian Mercury systems (Palo Alto, CA) at room temperature. ^1H NMR spectrums were referenced using Me_4Si (0 ppm), residual D_2O at δ ^1H-NMR 4.65 ppm. ^{31}P-NMR was used to evaluate the phosphorous groups from β-GP.

2.6 Histology and imaging

After 12 weeks, the animals were euthanized using CO_2 asphyxiation and cervical dislocation to allow confirmation of microCT imaging. The calvaria were harvested fixed, decalcified and paraffin embedded as described previously [20-22]. The embedded tissues were sectioned using a microtome to 6 µm thin sections and stained with Pentachrome, Hematoxylin and Eosin dyes for analyzing neo-vessel formation, mineralization, and bone morphology. For vascularization

analysis, samples were immunostained for CD31 and evaluated for microvessels as described previously [23]. The sections were then mounted and imaged with a bright-field microscope (Nikon).

2.7 Ultrasound imaging-guided in-vivo injection of microtissue

A 4-mm critical-sized calvarial defect was made, and skin was immediately sutured as detailed above. As a proof-of-concept, the microtissues were injected to the defect using a 23 gauge needle guided by ultrasound imaging. Before the procedure, the animal was euthanized using CO_2 asphyxiation to reduce pain and suffering. The animal was placed on the examination stage and imaged with a high-resolution small animal ultrasound unit, Visualsonics Vevo 770 (Visualsonics, Toronto, Canada). Hair was removed from the skin above the calvarial defect, and the acoustic gel was applied to couple the skin with the ultrasound probe. The microtissue were injected into the defect with a 23 gauge needle while the procedure was being recorded with the Vevo 708 scan head (55 MHz center frequency; 20-75 MHz -6 dB bandwidth; 30 µm axial resolution; 70 µm lateral resolution; 4.5 mm focal distance; 1.5 mm -6 dB focal depth; 100% transmit power) at a frame of 11 frames/s. 3D images of the defect before and after the injection was acquired by moving the ultrasound probe with a step size of 30µm over an 8 mm range while scanning. Spectral ultrasound analysis was done to discriminate the native tissues and microtissue construct based on their mineral content. Grayscale values GS(y,z), acoustic scatterer diameter and acoustic concentration were extracted from the raw backscattered radio-frequency (RF) signals as described previously [24].

To obtain the GS values, the backscattered RF data was Hilbert-transformed into complex analytical signal p(y,z) and then GS(y,z) was determined as the logarithm of the amplitude envelop of the signal:

$$GS(y,z) = \log_{10}|p(y,z)|.$$

Grayscale images were reconstructed using the GS value for each pixel, and the mean absolute values of GS(y,z) over the region of interest was determined for each frame.

For power spectrum analysis, each of the RF scan line was segmented by a 0.2 μs hamming window sliding with an offset of 0.1 μs and processed by taking the Fast Fourier Transform. For removing the system and operator dependency, the gated power spectrum was then normalized by a calibration power spectrum obtained from imaging an oil-water interface, a perfect reflector. A linear fit was applied to the calibrated gated power spectrum within a -9 dB bandwidth to determine the slope (m) and mid-band fit (MBF). The effective scatterer diameter (a) was calculated from the slope (m), the geometry index (n), the center frequency of the imaging transducer (f_c), and bandwidth of the transducer (b), and is given by:

$$a = 2 * \sqrt{0.25n\frac{[b-(1-\frac{b^2}{4})]}{b^3 f_c^2} - \frac{m}{105.5 f_c}}.$$

The scatterer concentration, CQ^2, is defined as the product of scattering concentration and the square of the acoustic impedance of the scatters and depends on the MBF, scatterer diameter (a) and a shape dependent factor (E) as:

$$CQ^2 = \frac{\exp(0.23\left(MBF - g_1 n - g_2(\frac{a}{2})^2\right))}{Ea^{2(n-1)}}, \text{ where}$$

$$g_1(f_c, b) = 4.34[\ln(f_c\left(1-\frac{b^2}{4}\right)^{0.5}\left(\frac{2+b}{2-b}\right)^{\frac{1}{b}}) - 1],$$

$$g_2(f_c, b) = -76.9 f_c^2(3 + \frac{b^2}{4}).$$

The mean value of the scatterer diameter (a) and the acoustic concentration (CQ^2) in decibel scale over the region of interest were determined for each frame and reported as the average scatterer diameter (ASD) and average acoustic concentration (AAC) respectively. Parametric images were created by overlaying the grayscale image with the scatterer diameter (a) and the acoustic concentration (CQ^2) for each pixel.

2.8 Statistical analysis

All measurements were performed at least in triplicate. Data are plotted as means with error bars representing the standard deviation. Statistical comparisons were made using Student's *t*-test and two-way ANOVA with a 95% confidence limit. Differences with $p<0.05$ were considered statistically significant.

Results

3.1 Fabrication and characterization of chitosan-collagen osteogenic microtissues

First, we screened the chitosan-collagen (CHI-COL) hydrogel formulation that can create stable microtissues and found that 0.2 % collagen-0.25 % chitosan exhibited minimal contraction (**Supplementary Figure. 1A**) after the addition of glyoxal and β-glycerophosphate while promoting early osteogenesis (**Supplementary Figure. 1B**). Then, the ideal formulation was used to fabricate microtissues using water-in-oil emulsification method (**Fig. 1A**). The chosen CHI-COL hydrogel formulation without any cells yielded microtissues with an average diameter of 54.3±12.1 µm after emulsification. The inclusion of cells or HA particles increased the size of the microtissues (**Fig. 1B**). Hydrogels with 0.5 million cells/ml yielded microtissues with an average diameter of 84.6 ±18.2 µm. Increasing the cell density (> 0.5 million cells/ml) reduced the number

of acellular beads, but the average diameter of the cell-laden microtissues remained constant. Our preliminary in vivo calvarial implants of the CHI-COL microtissues with MSC couldn't completely heal the defect with calcified bone (**Supplementary Figure. 2**). Therefore, to enhance calcification, HA nanoparticles were added to the CHI-COL composite. The inclusion of HA (200 nm dia) increased the size of the microtissue that varied with the amount of HA content (**Supplementary Figure. 1C**). The diameter of 0.5%, 1% and 2% HA CHI-COL microtissues were 73.9±17.7 µm, 79.7±18.7 µm, and 148.6±21.4 µm respectively (**Fig. 1C)**. The inclusion of 0.5 million cells/ml along with 1% HA didn't significantly change the size (81.1±20.1 µm, **Fig. 1C)**. In vitro characterization of microtissues showed robust osteogenesis of MSC under osteogenic conditions (**Fig. 1D)**. Further, the NMR analysis of the microtissues confirmed the presence of both collagen and chitosan (**Fig. 1E)**. The composition of the microtissues stayed the same for up to 21 days under culture conditions (**Supplementary Figure. 3**).

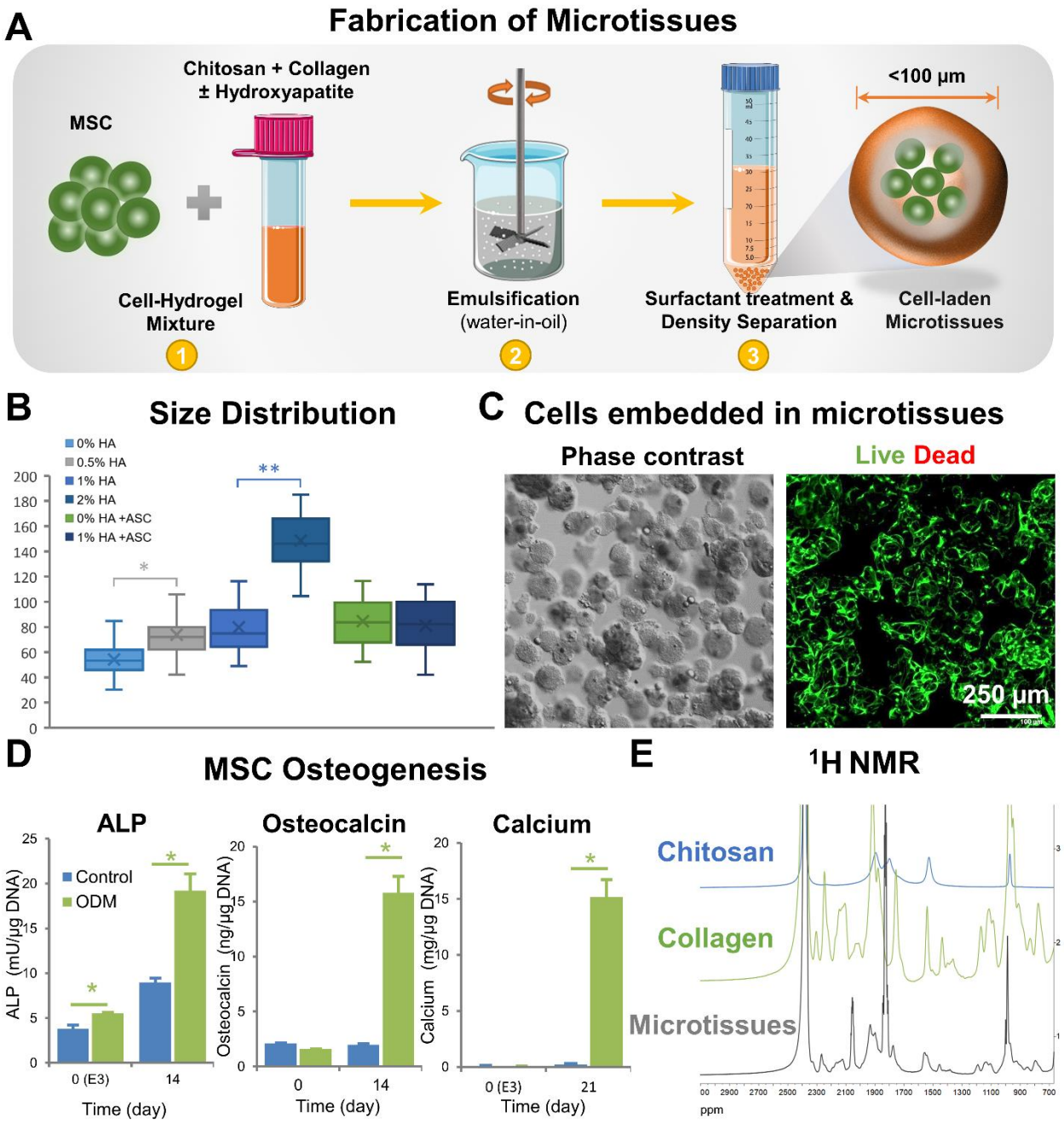

Figure.1 Fabrication and characterization of chitosan-collagen osteogenic microtissues.
(A) Fabrication of osteogenic microtissues through water-in-oil emulsification of chitosan-collagen composite hydrogel. (B) Size distribution of CHI-COL microtissues made with different hydrogel composite preparations. The inclusion of MSC or HA nanoparticles (200 nm diameter) increase the size of the microtissues. (C) Phase contrast image of CHI-COL microtissues containing 0.5x10^6 cells/mL of hydrogel shows uniform size distribution and a spherical morphology. The live/dead staining at 1-week culture shows robust MSC cell viability. (D) In vitro characterization of microtissues shows robust osteogenesis of MSC under osteogenic conditions. (E) The NMR analysis of the microtissues shows the presence of both collagen and chitosan.

3.2. Bone regeneration in critical-sized calvarial defect

We investigated the bone regeneration potential of microtissues fabricated with 1) no cells; 2) non-predifferentiated-MSC (MSC); and 3) osteogenically-predifferentiated MSC (OD-MSC), in a mouse full-thickness critical-sized (4-mm diameter) cranial defect. Microtissues made from 1.0 ml of initial hydrogel volume was implanted in the defect, and the bone regeneration in the defect was monitored through µCT analysis at week 5, 10 and 15. Gross examination of the 3D reconstructed µCT images showed that by week 10, the OD-MSC microtissues had bridged >95% of the defect area ($p<0.001$, **Fig. 2A**). In contrast, microtissues with MSC showed significantly less bony bridges ($p<0.05$) with ~50% coverage and microtissues without cells showed the lowest bridging of the defect measuring only ~30% of defect area (**Fig. 2A** and **Supplementary Figure. 4)**. Correspondingly, the total bone volume, bone mineral content, bone mineral density and bone volume fraction (bone volume/tissue volume) of the newly formed bone in the 4-mm defect was significantly higher in the OD-MSC microtissues compared to other conditions (**Fig. 2B-E**, $p<0.001$). Histomorphometric analysis of the newly formed bone in osteogenically-pre-differentiated samples revealed lamellar and woven bone morphology, high collagen deposition (yellow staining) and marrow cavity-like structures (**Fig. 2F**). The MSC microtissues also had minimal bony apposition at the defect borders and few bone spicules surrounded by fibrous connective tissues. Additionally, the MSC microtissues showed the lowest collagen deposition. The microtissues without cells had the lowest mineral content, but the defect was fully bridged with collagenous osteoid structures interspersed with blood vessels (**Fig. 2F**).

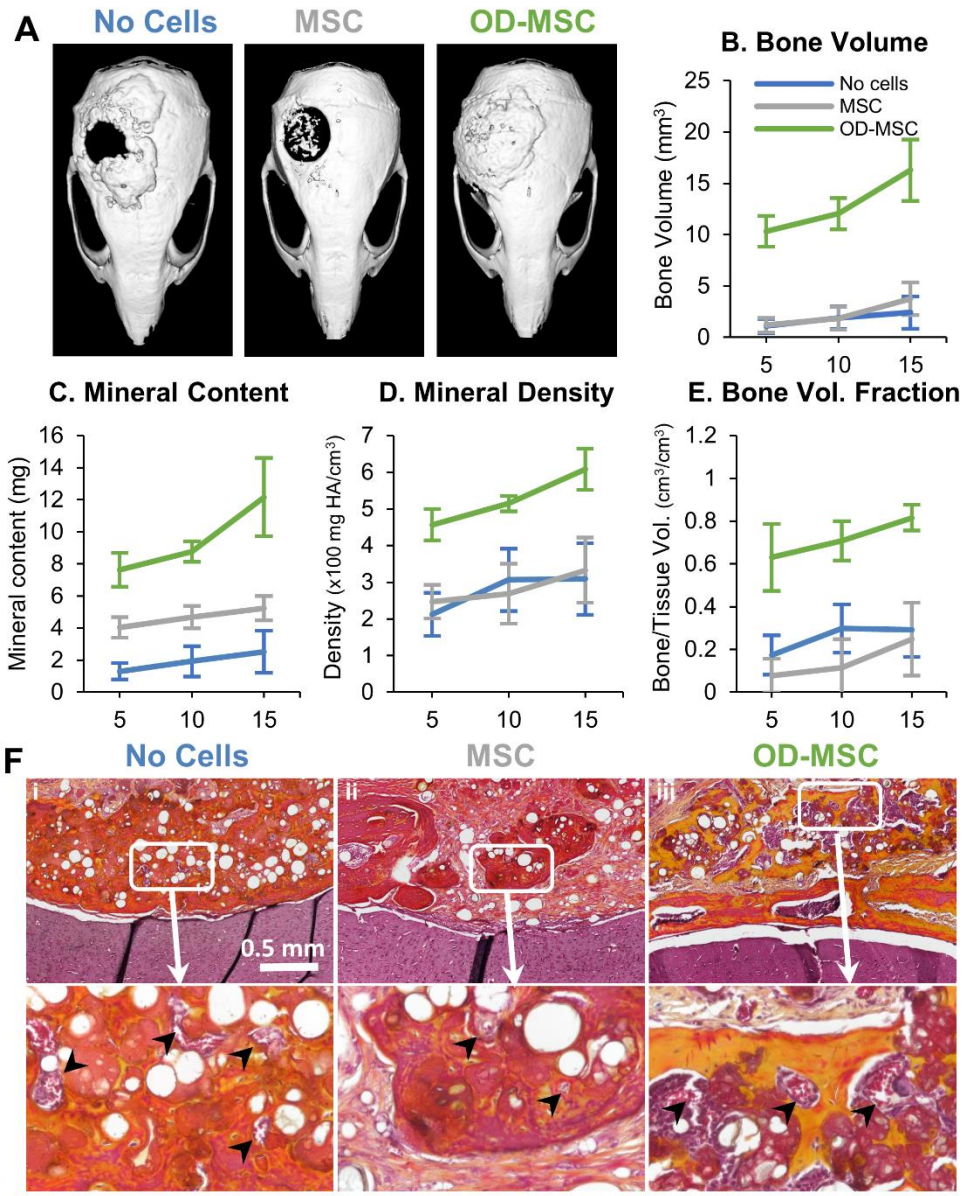

Figure.2 Bone regeneration in the critical-sized calvarial defect. (A) *The week 10 µCT images show new bone formation in and around the defect. The OD-MSC microtissues bridged >95% of the defect area (p<0.001). The microtissues with MSC showed significantly less bony bridges (p<0.05) with ~50% coverage, and microtissues without cells showed the lowest bridging of the defect measuring only ~30% of defect area. (B) The total bone volume, (C) bone mineral content, (D) bone mineral density and (E) bone volume fraction (bone volume/tissue volume) of the newly formed bone in the 4-mm defect was significantly higher in the OD-MSC microtissues compared to other conditions (p<0.001). (F) Histomorphometric analysis of the newly formed bone in the defect: (i) The microtissues without cells had the lowest mineral content compared to other groups, but the defect was fully bridged with collagenous osteoid structures interspersed with blood vessels; (ii)The MSC microtissues also had minimal bony apposition at the defect borders and few bone spicules surrounded by fibrous connective tissues and showed the lowest collagen deposition; (iii) OD-MSC samples revealed lamellar and woven bone morphology, high collagen deposition (yellow staining) and marrow cavity-like structures.*

3.3. Cell density and microtissue volume influence bone formation

Although OD-MSC microtissues supported the robust bone formation and bridged the critical-sized defect, the microtissues and hence the newly created bone was not always contained within the defect. To contain the newly formed bone within the defect, the total microtissue volume and cell density on bone regeneration were modified and examined. Further a 10 µL fibrinogen solution (8 mg/ml of PBS) and 10 µL of thrombin (50 U/mL) solution were applied on top of the implants in-situ, to hold the position of the construct. Three types of implants (low, medium and high volume) containing OD-MSC microtissues made from 0.75 mL, 0.50 mL and 0.25 mL of initial hydrogel volume respectively were studied. The cell density was kept constant in all conditions at 0.5×10^6 cells/mL of the hydrogel. The µCT scan of the defect obtained at time 0, 3, 6, 9 and 12-week time points show that the new bone volume decreased with reduction in the amount of microtissues implanted (**Fig. 3A**). Although no statistical difference in bone volume (**Fig. 3B**) between high and medium volume conditions was noticed, it dropped significantly with low volume (0.25 mL) implants. A similar downward trend was seen in the bone mineral content (**Fig. 3C**), bone mineral density (**Fig. 3D**) and bone volume fraction (**Fig. 3E**) with a decrease in total microtissues volume. Consistent with the radiographic analysis, the histomorphometric analysis of the calvaria at 12-week showed a reduction in lamellar and woven bone formation with a decrease in total microtissue volume (**Fig. 3F**).

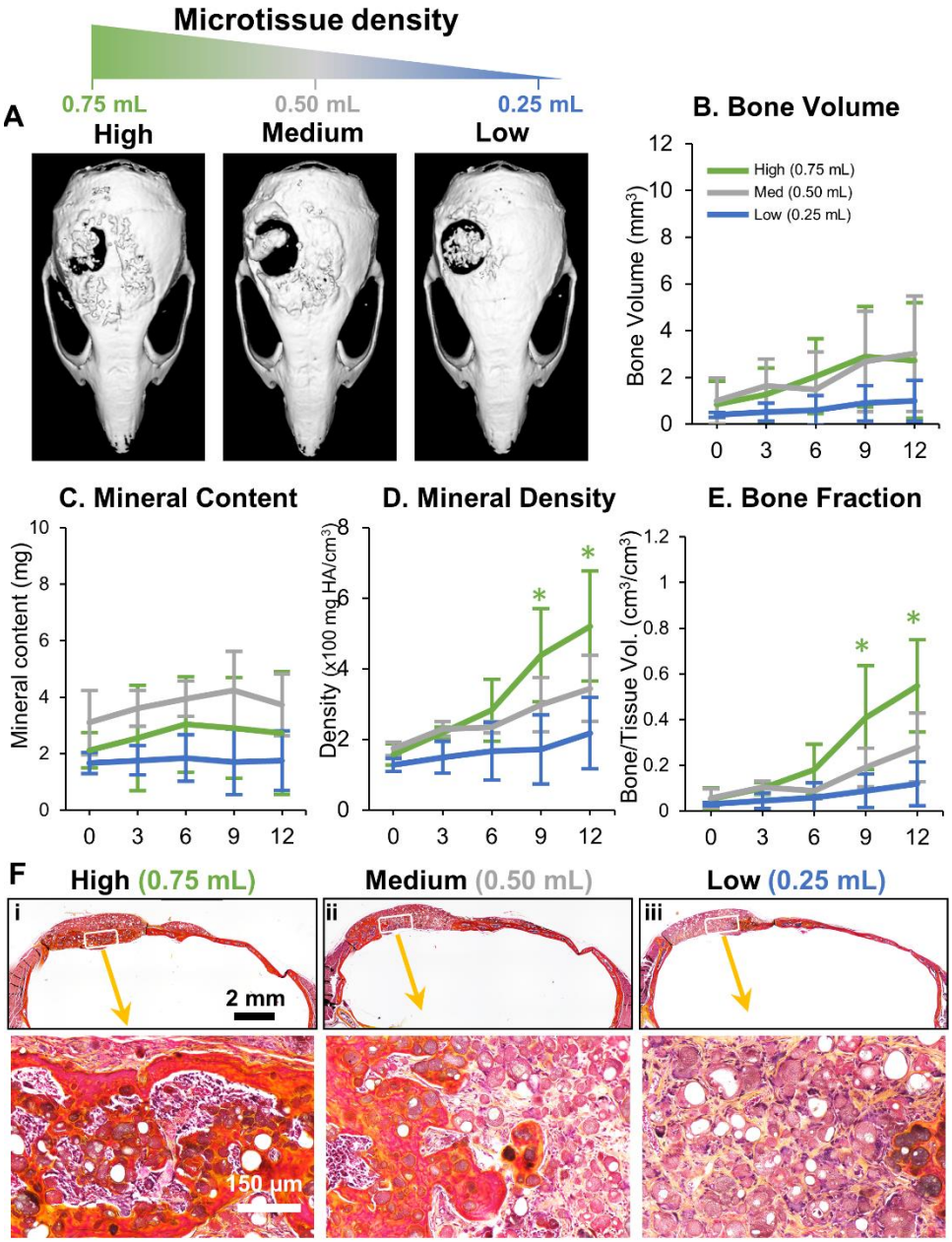

Figure. 3 Influence of microtissue density on bone formation. *(A) The µCT scans of the defect obtained 12 weeks after implantation show that the new bone volume decreased with reduction in the amount of microtissues implanted. (B) No statistical difference in bone volume between high and medium microtissue volume conditions was noticed. But the bone volume is significantly low in the group with low volume (0.25 mL) implants. A similar downward trend was seen in the bone mineral content (C), bone mineral density (D), and bone volume fraction (E) with a decrease in total microtissues volume. (F) The histomorphometric analysis of the calvaria at 12-week showed a reduction in lamellar and woven bone formation with a decrease in total microtissue volume.*

The influence of cell density of microtissues in regenerating bone was investigated while keeping the implant volume constant (microtissues made from 1 mL of initial hydrogel volume). Three types of implants (low, medium and high cell density) containing OD-MSC microtissues with $1x10^6$, $2x10^6$ and $3x10^6$ cells/mL of initial hydrogel volume respectively were studied. Interestingly, increase in cell density reduced the ossification of microtissues and formation of bony structures in the defects (**Fig. 4A**). Higher cell densities had significantly reduced new bone volume (**Fig. 4B**), bone mineral content (**Fig. 4C**), and total bone fraction (**Fig. 4E**), while the lowest cell density ($1x10^6$ cells/mL of hydrogel) consistently outperformed the medium- and high-density implants in all metrics. The bone mineral density, however, stayed the same between the groups (**Fig. 3D**). The histomorphometric analysis showed lamellar and woven bony structures with collagen deposition within the defect in all conditions, but more ossified regions were seen in implants with low cell densities (**Fig. 3F**).

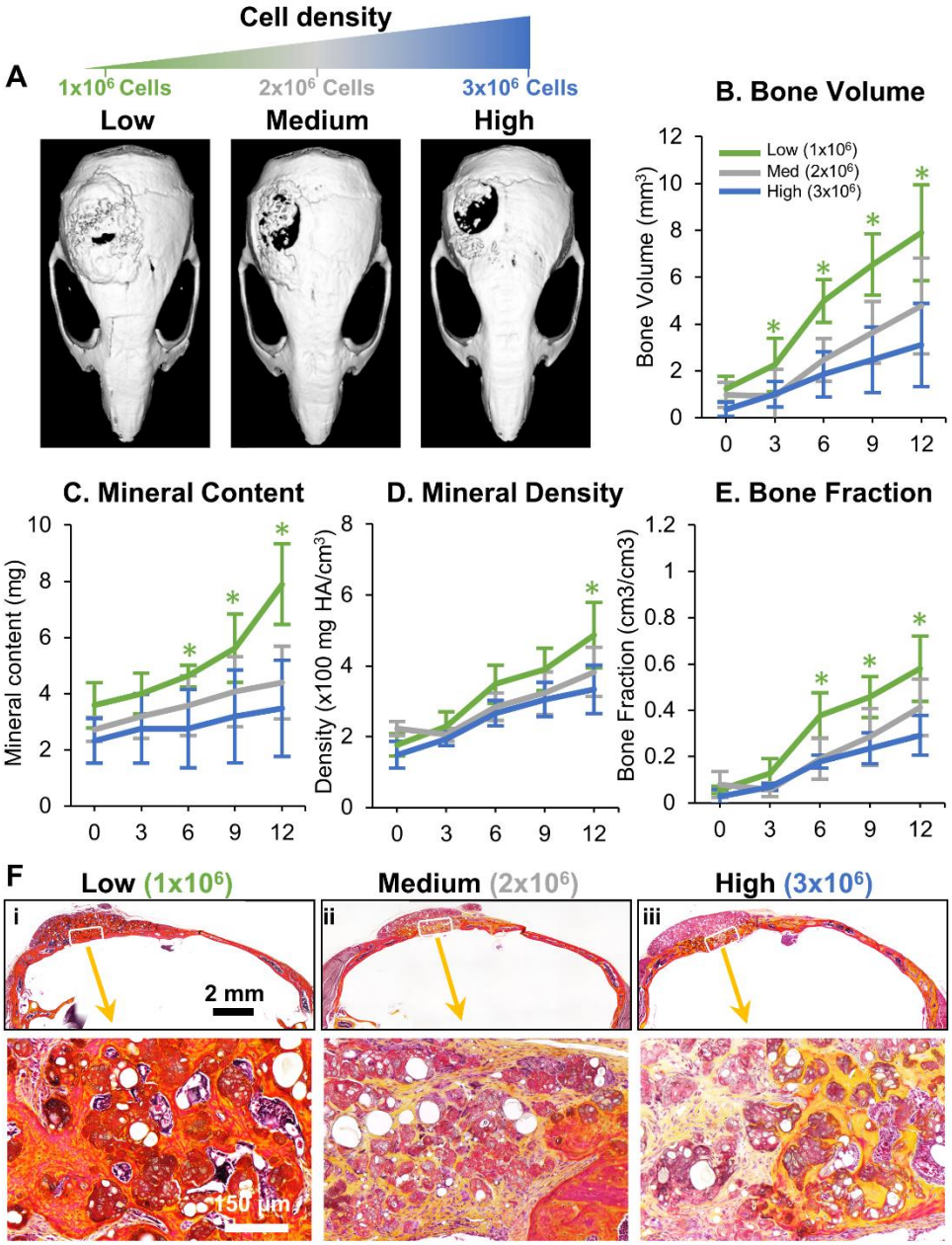

Figure. 4 Influence of microtissue volume on bone formation. *(A) The µCT scans of the defect obtained 12 weeks after implantation show that the increase in cell density reduced the ossification of microtissues and the formation of bony structures in the defects. Radiographic analysis shows that the implants with higher cell densities had significantly reduced new bone volume (B), bone mineral content (C), and total bone volume fraction (E), while the implant with lowest cell density (1x10^6 cells/mL) consistently outperformed the medium- and high-density implants in all metrics. (D) No significant variation in bone mineral density was seen between the groups. (F) The histomorphometric analysis showed lamellar and woven bony structures with collagen deposition within the defect in all conditions, but more ossified regions were seen in implants with lower cell densities.*

3.4. Fibrin carrier gel concentrates microtissues within the defect

To hold the microtissue and prevent excess bone growth outside the defect area, the microtissues were embedded in a carrier fibrin gel before implantation. Unlike the previous study where the construct was coated with 10 µL fibrin solution, the microtissues in this experiment were suspended in excess fibrin hydrogel solution before casting the bulk construct. Healing potential, defect containment, and conformity of the OD-MSC implants made with carrier gel was investigated and compared to that of the implants without carrier gel. Non-predifferentiated MSC implants served as control. The µCT showed that the carrier gel helped to contain the microtissues within the defect while conforming to the defect area (**Fig. 5A**). Within nine weeks the defect was bridged entirely in both the OD-MSC conditions with evidence of active remodeling. The µCT analysis showed that the new bone volume was higher in OD-MSC with carrier gel at week 12 compared to that of OD-MSC implants without a carrier gel (**Fig. 5B**). There is no significant difference in bone mineral density, bone mineral content and bone volume fraction between the two (**Fig. 5C, D, F**). Histomorphometric analysis showed collagenous lamellar and woven bone formation in OD-MSC implants (**Fig. 5E**) with significantly higher vessel area compared to MSC condition (**Fig. 5G**). The newly formed collagenous bone had well-developed blood vessels (Fig. **5H**). The control MSC implants exhibited poor ossification and had no bony structure. Fluorescent imaging of the calvaria using an in vivo imaging system (IVIS® Spectrum) and confocal microscope (Nikon A1) showed the presence of the red-fluorescent exogenous mTmG MSC in all conditions (**Supplementary Figure. 5**), confirming the engraftment of the supplied MSC.

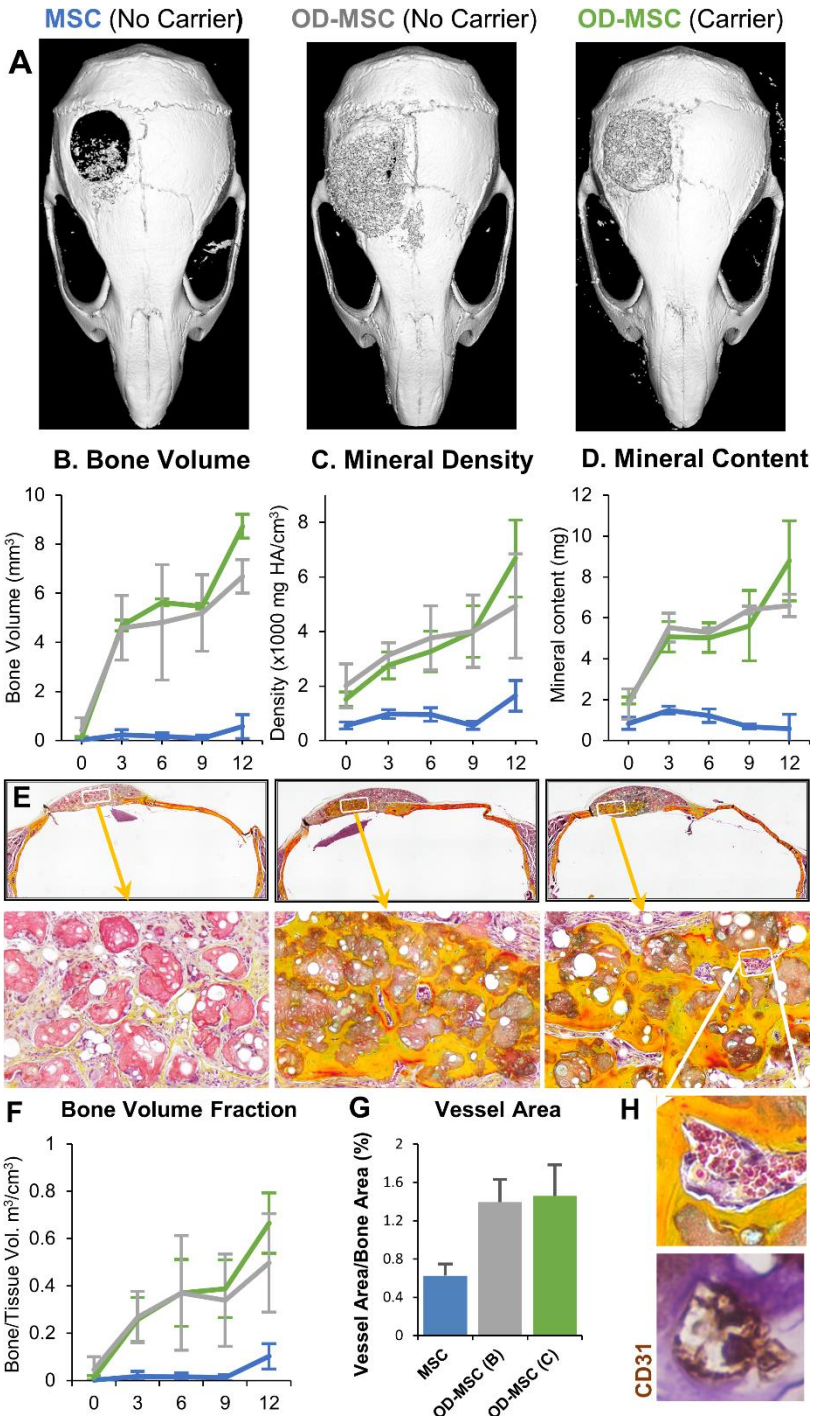

Figure.5 Fibrin carrier gel to concentrate microtissues within the defect. *(A)The week-12 µCT images of the calvaria show that the carrier gel helped to contain the microtissues within the defect while conforming to the defect area. (B) The radiographic analysis shows that the new bone volume in the defect is higher in OD-MSC with carrier gel at week 12 compared to that of OD-MSC implants without a carrier gel. However, there is no significant difference in bone mineral density (C), bone mineral content (D), and bone volume fraction (E) between the two groups. (F) Histomorphometric analysis showed collagenous lamellar and woven bone formation in both OD-MSC groups. (G) Significantly higher vessel area was also seen in OD-MSC implants compared*

to MSC implants. (H) Immunohistochemistry of the tissue sections shows that the newly formed collagenous bone had well-developed blood vessels in the OD-MSC implants.

3.5. Ultrasound-guided minimally invasive delivery of microtissues

Finally, to demonstrate the injectability, the microtissues were administered through a 23-gauge hypodermic needle to the 4-mm calvarial defect guided by a high-resolution spectral ultrasound imaging in real-time (**Fig. 6A, See Supplementary** file for the real-time movie). The microtissues were injected into the defect while the procedure was being imaged and recorded with a 55 MHz scan head. Ultrasound imaging at high frequency (55 MHz) enabled the creation of 3D spatial maps of the defect and the surrounding tissues. 3D images of the defect area at different time points during the procedure was acquired by moving the ultrasound probe with a step size of 30 µm over an 8 mm range. **Fig. 6B** shows the step-wise 3D reconstructed spatial map of the defect being filled with the microtissues. Moreover, the spectral ultrasound imaging (SUSI) can also be used to quantify the mineral content of the implanted tissues. A plot of the mineral content of the microtissues versus spectral parameter, Midband fit (dB), shows a linear correlation (**Fig. 6C**) and hence can discriminate tissues based on their mineral content. The acoustic concentration also shows the increase in the mineral concentration of the constructs (**Fig. 6D, Supplementary Figure. 6**). This non-destructive ultrasound imaging can be used for quantitative and longitudinal monitoring of implant ossification and defect healing.

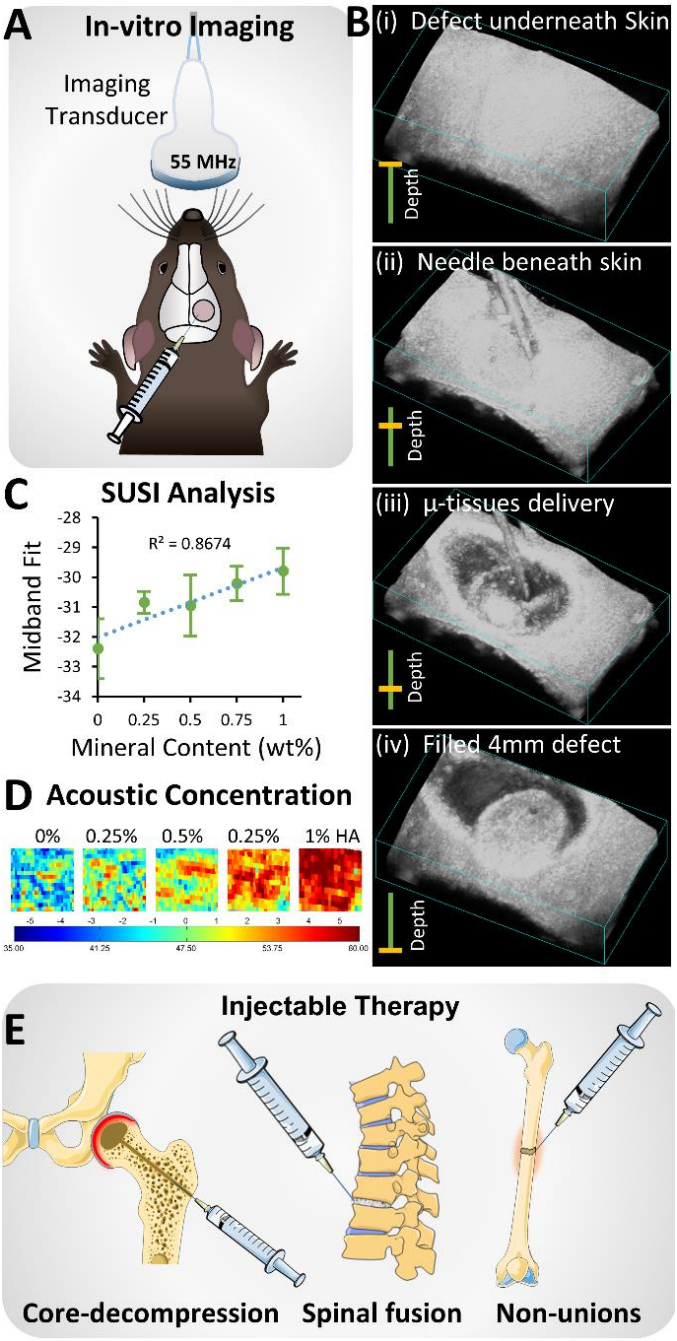

Figure.6 Ultrasound-guided minimally invasive delivery of microtissues. *The injectability of the microtissues was demonstrated by administered them through a 23-gauge hypodermic needle to a 4-mm calvarial defect guided by a high-resolution spectral ultrasound imaging in real-time. (A)A schematic of the procedure showing the microtissues being injected into the defect while the procedure was being imaged and recorded with a 55 MHz scan head. (B) Ultrasound imaging at high frequency (55 MHz) enabled the creation of 3D spatial maps of the defect and the surrounding tissues. The step-wise 3D reconstructed spatial map of the defect being filled with the microtissues is shown. (C) The spectral ultrasound imaging (SUSI) can also be used to quantify the mineral content of the implanted tissues. A plot of the mineral content of the microtissue implants versus spectral parameter, Midband fit (dB), shows that Midband fit is linearly correlated with the mineral concentration. (D) Image of acoustic concentration for samples containing 0.0 to 1.0 wt% HA, shows that the acoustic concentration increases with increasing mineral concentration. (E) Clinical procedures such as spinal fusion, core decompression, non-unions, cyst removal, and craniofacial procedures can benefit from our modular approach that employs injectable microtissue to make moldable bioartificial constructs.*

4. *D*iscussion:

There have been tremendous advances in orthopedic implants and surgical methods for bone reconstruction over the past decade. However, there has been a lot of inconsistency between the clinical demand for the technology and its clinical translation. The desired properties of a tissue-

engineered bone substitute depend on the intended clinical use. For instance, large load-bearing bones require constructs with high mechanical stability. However, in case of unopened fracture with bone loss, initially, injectable constructs are advantageous [25, 26]. Such conditions can benefit from a modular approach that employs injectable microtissue to make moldable bioartificial constructs (**Fig. 5E**). Furthermore, an autologous source for skeletal stem cells is very desirable to eliminate immune complications. We used adipose MSC which can be easily obtained from the stromal vascular fraction of lipoaspirate [27]. They are described as mesodermal stromal cells, with verified potential to differentiate into osteogenic, chondrogenic, adipogenic and myogenic lineages among other [28-31]. They are highly proliferative and possess robust mineralization capabilities [17, 32]. In this study, we combined these adipose-derived MSC with chitosan, collagen and hydroxyapatite particles to create osteogenic microtissues. The osteogenic microtissues were first characterized in-vitro and found to be biocompatible and support MSC mineralization (Fig. 1). Since the composition of the microtissues can be customized, they can be tailored for various applications. We specifically tweaked the composition to enhance osteogenic potential of the microtissues. To enrich the mineralization potential of these microtissues, we also included hydroxyapatite particles. Further, the size of the microtissues can be varied depending on the hydrogel composition and emulsification conditions [33]. Then we proceeded to investigate the in-vivo performance of the microtissues in a murine critical-sized calvarial defect.

Our study sought to investigate the potential of our modular constructs to bridge the critical-sized defect completely. We also studied the influence of the exogenously supplied MSC and their differentiation state in healing the defect. Microtissues implanted without cells created mineralized bone in apposition to the native bone but only formed collagenous osteoid within the defect (by week 15). Although they couldn’t bridge the defect with mineralized bony structures, poorly-

mineralized osteoid spanned the full defect. Interestingly, microtissues with MSC exhibited less collagen deposition but had islands of calcified bone in the defect (by week 15). The total new bone volume, within the defect, in MSC condition was not significantly higher than that of the acellular microtissues. Nonetheless, the microtissues with osteogenically-predifferentiated MSC (OD-MSC) formed robust collagenous woven bone which completely bridged the defect. The inability of non-predifferentiated MSC to bridge the defect may be related to their immunomodulatory potential. Several clinical studies have shown that MSC have anti-inflammatory and immune-privilege potential [34]. Similar to bone marrow-derived MSC, adipose-derived MSC lack HLA-DR (of MHC class II) [35], an antigen commonly implicated in graft loss. Also, they can suppress lymphocyte reactivity by secreting prostaglandin E2 (PGE2) and reduce inflammation in vivo [36]. Studies have also shown that MSC reprogram monocyte/macrophages to an anti-inflammatory phenotype via PEG-2 secretion [37, 38]. Although this phenomenon can be beneficial to avoid graft-vs-host diseases, they can suppress other pathways including ossification that relies on pro-inflammatory signals. It has been reported that the osteogenic commitment of adipose-MSC is primarily controlled through extracellular signal-related kinase (ERK) pathway and its interruption can inhibit osteogenic differentiation [39]. Interestingly, a key pro-inflammatory cytokine: tumor necrosis factor-alpha (TNFα) has shown to be an activator of ERK and plays a critical role in the osteogenic commitment of adipose-MSC [40]. Further TNFα has also been shown to induce osteogenesis through the activation of NF-κB [40]. Another inflammatory cytokine IL-6, secreted by monocytes/macrophages is also shown to stimulate osteogenesis and bone formation [41]. Collectively, the immunosuppression by non-predifferentiated MSC could be inhibiting the secretion of inflammatory cytokines which in turn suppress MSC osteogenesis. Although some studies have reported bone formation without

MSC preconditioning, often the graft is repopulated with host cells while the exogenously supplied cells undergo apoptosis rapidly [17]. These scaffolds will likely fail in more substantial defects that lack functional vasculature as seen in some clinical studies [42]. Since our modular approach can enhance mass transport and accelerate neovascularization [43], apoptosis of implanted MSC are greatly reduced, and hence the MSC immunosuppression is maintained. Some strategies circumvent stunted ossification by priming MSC with BMP2 [44], TNFα [45] and other osteogenic cytokines [46]. In fact, MSC partially differentiated to osteoblasts (using dexamethasone and β-glycerophosphate) are shown to recruit macrophages and improve cranial defect in a murine model [47]. Similarly, we primed the MSC with dexamethasone, a commonly used *Runx2* regulator [48], along with β- glycerophosphate as the phosphate source. The priming step yielded robust in-vivo MSC ossification, neovascularization, and defect healing.

Since the newly formed bone was not always contained within the defect, we tested constructs with reduced volume of microtissues. We found that decreasing the total microtissues volume had some impact on containing the construct within the defect. But, it caused reduced lamellar bone formation, mineral deposition, and remodeling. Then we tested constructs with increasing cell densities while keeping the total volume of the microtissues constant. Interestingly, the increase in cell density caused a decrease in bone formation and remodeling. The lowest cell-density constructs displayed woven bone morphology and marrow-like tissues with substantial bone formation. But the high-density constructs showed reduced bone formation and remodeling. This is likely due to the necrosis of the microtissues at high cell densities. Although hypoxia-induced preconditioning is shown to enhance survival and osteogenic potential of MSC [49-51], the severity of hypoxia determines whether the cells become necrotic or adapt to hypoxia and

persist [52]. Therefore, maintaining an appropriate cell density and subsequent hypoxic level is indispensable to maximize the regenerative potential of MSC.

Modifying cell density and the microtissue volume enabled to have some control over microtissue, however the construct is not completely retained within the defect. Then, we tried to suspend the microtissues in a polymerizable fibrin gel to restrict them within the defect. We chose the clotting protein fibrinogen as a suitable carrier gel for its efficacy in promoting angiogenesis and vasculogenesis [53, 54]. Fibrinogen is a crucial protein that undergoes thrombin-mediated polymerization to form insoluble fibrin matrix, and it can be easily isolated from patient's blood. Fibrin material can be easily manipulated and has been widely investigated as a matrix for creating vascularized tissues including bone [55, 56]. The ease of handling, vasculogenic potential, and control over polymerization make fibrin an attractive carrier gel for delivering osteogenic microtissues. As expected the constructs with fibrin carrier gel were held inside the defects and reduced movement of the microtissues outside the defect area.

When compared to the non-carrier bound microtissues, the microtissues with carrier gel formed mature bone with same woven bone morphology, collagen deposition, and mineral content. They both had a substantial bone formation with numerous blood vessels by the end of week 12. However, the amount of microtissues supplied with the carrier gel group is only $1/10^{th}$ of the volume of microtissues implanted in no-carrier condition. This strategy not only saved the number of cells and materials but also contained the graft within the defect and reduced excess bone formation. This is clinically significant for creating a custom-fit and shape conforming construct. As a proof-of-concept, we also demonstrated the injectability of the microtissues with a non-invasive imaging modality. The ultrasound imaging uses the attenuation coefficients to discriminate different tissues [57]. Even without a carrier gel, the microtissues form a paste and

can be injected through a hypodermic needle with ease. These microtissues can be applied to various instances including for bone fracture, implant stabilization, and non-unions. Together, our findings in the report suggest that our injectable constructs provide a clinically applicable strategy for various bone defects. Further studies are necessary to investigate the efficacy of our approach in a load bearing and ischemic environment.

Summary/Conclusion:

Together, the study demonstrates that the injectable chitosan-collagen based microtissues can sufficiently conform to and bridge critical-sized defects with vascularized lamellar and woven bone. While the osteogenically primed MSC can accelerate bone regeneration, the naive MSC can enhance the immune tolerance of the implanted construct. Combining these two phenotypes can maximize the benefits, and further studies are necessary to verify the efficacy. Overall the microtissues can be used to augment the differentiated function of MSC, and to provide a suitable extracellular environment to promote bone repair and integration, while also allowing guided and minimally-invasive delivery to defect sites. The modular microtissue format can potentially be used for the engineering of other thick and solid tissues including liver, pancreas, cartilage, and large blood vessels with different combinations of cell types and biomaterials. In combination with biomolecule-delivery systems, the microtissues can be applied to modulate inflammation and to augment tissue repair. This microtissues approach could also be used for matrix-assisted cell delivery, augmentation of bioreactors and cell-based extracorporeal devices.

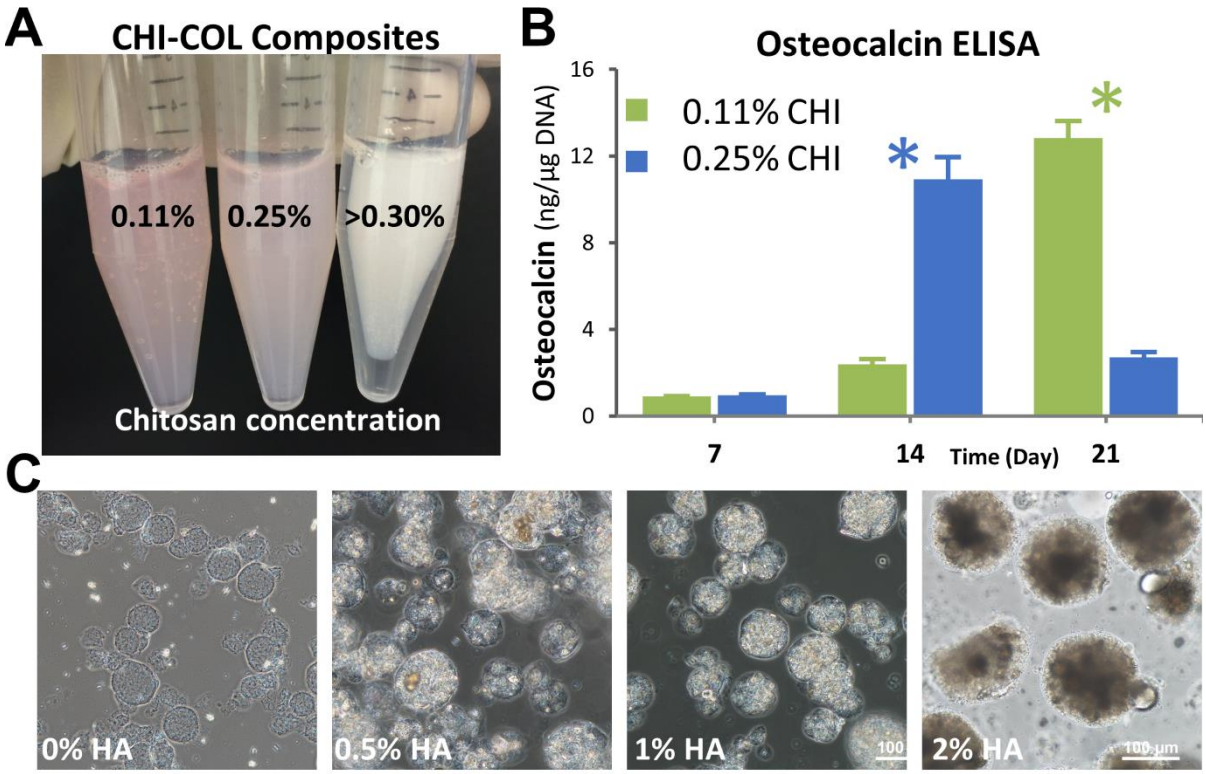

Supplementary Figure. 1 Screening of chitosan-collagen microtissue formulation. *(A) Chitosan-collagen (CHI-COL) hydrogel formulation that can create stable microtissues was screened. The composite made up of 0.2 % collagen, and 0.25 % chitosan exhibited minimal contraction after the addition of glyoxal and β-glycerophosphate (B) Early peak in the expression of osteocalcin by day 14 in 0.25% chitosan composite indicated an increase in osteogenicity of microtissues with an increase in chitosan concentration. Based on our screening 0.2% collagen-0.25% collagen hydrogel composite was deemed suitable for fabricating osteogenic microtissues through emulsification. (C) The inclusion of HA particles increased the size of the microtissues. The acellular microtissues (0% HA) had a diameter of 54.3±12 µm while the diameter of 0.5%, 1% and 2% HA CHI-COL microtissues were 73.9±17.7 µm, 79.7±18.7 µm, and 148.6±21.4 µm respectively.*

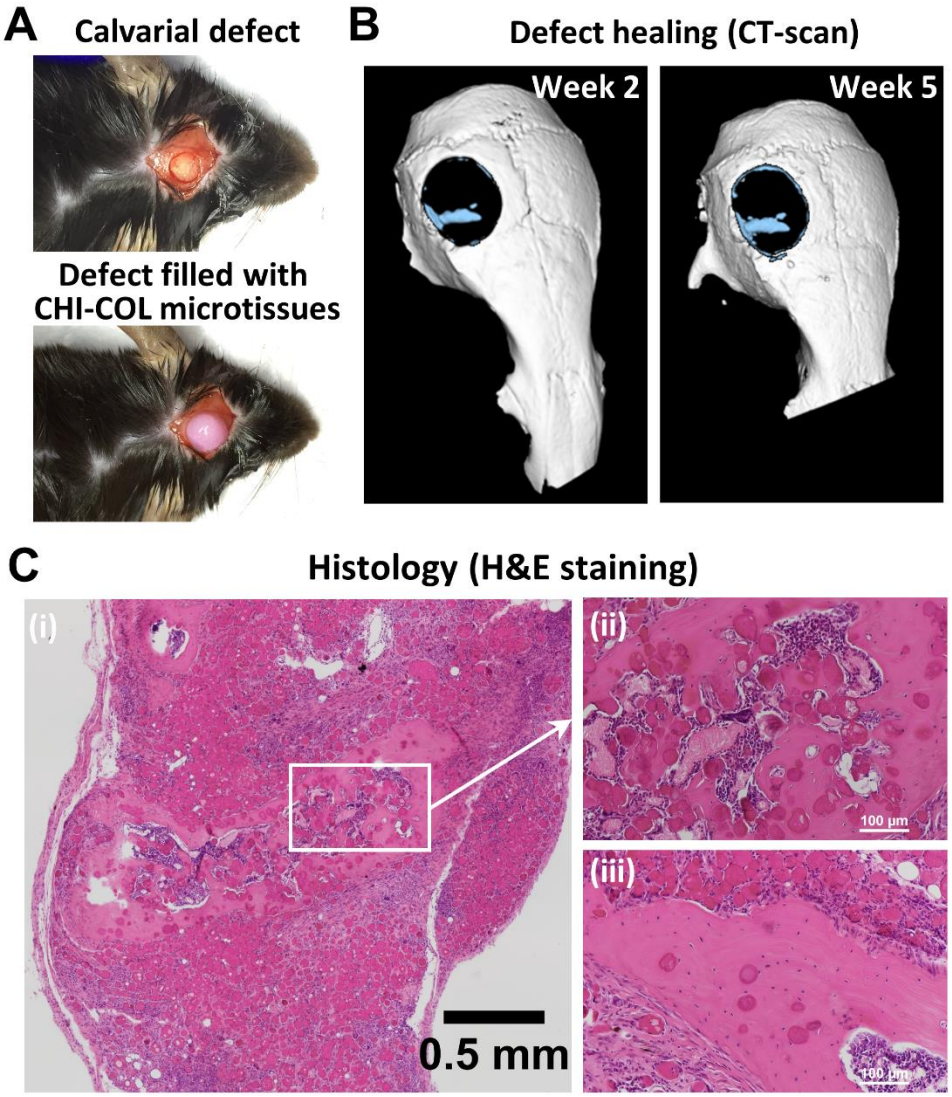

Supplementary Figure 2 In-vivo characterization of COL-CHI microtissues without HA. *(A) A unilateral 4 mm full-thickness critical-sized calvarial defect was created using a diamond-coated trephine bit in the non-suture associated right parietal bone, taking care to avoid dural injury. The implant was squirted to fill the defect, and the skin was sutured immediately. (B) The µCT scan of the defect at weeks 2 and 5 showed very low ossification and wound closure. (C) Histological analysis of calvarial samples at week-6. (i) The H&E staining of the sections revealed areas of the lamellar bone formation with remnants of the microtissues embedded within the structure (ii) and (iii). However, CHI-COL microtissues with MSC couldn't completely heal the defect with calcified bone.*

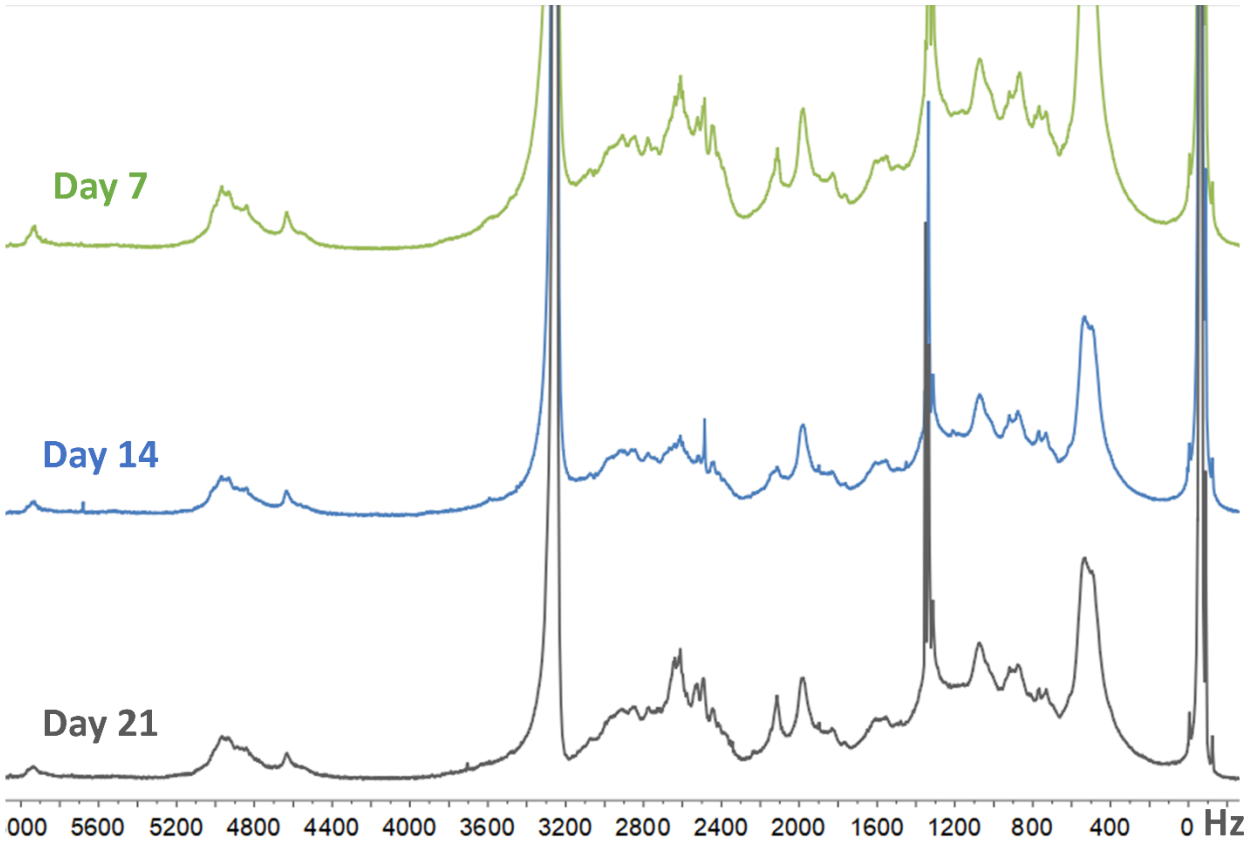

Supplementary Figure 3 Temporal analysis of microtissues chemical structure using NMR analysis. *The chemical composition of the microtissues seeded with MSC stayed intact and showed the presence of both collagen and chitosan for up to 21 days under culture conditions.*

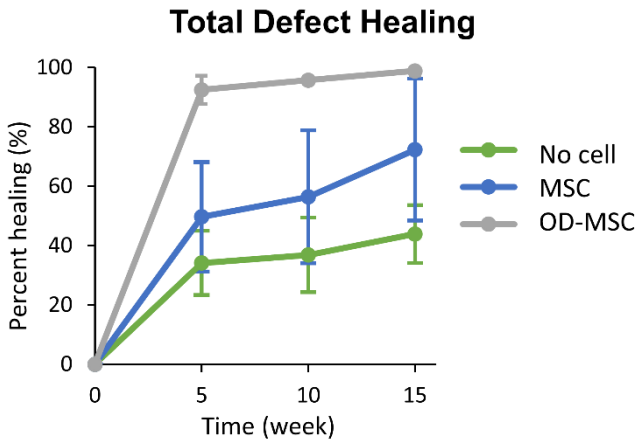

Supplementary Figure 4 Quantification of defect healing through image analysis. *Gross examination of the 3D reconstructed µCT images showed that by week 10, the OD-MSC microtissues had bridged >95% of the defect area. In contrast, microtissues with MSC showed*

only ~50% coverage, and microtissues without cells showed the lowest bridging of the defect measuring only ~30% of defect area.

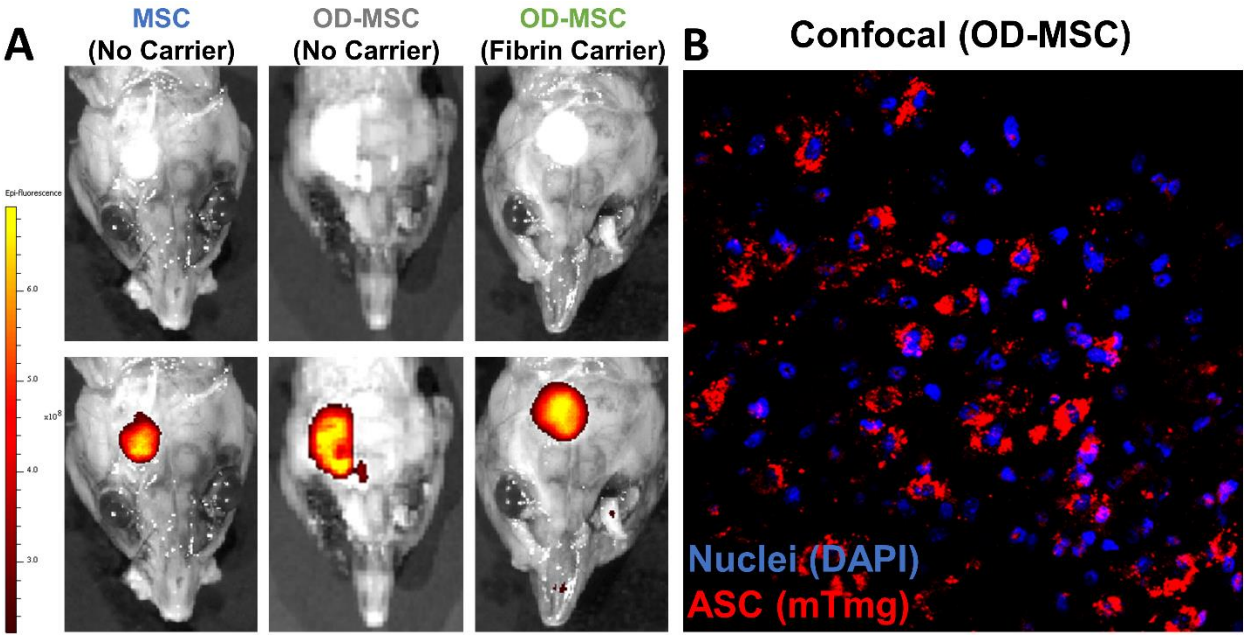

Supplementary Figure 5 Fluorescent imaging of the implanted MSC within the constructs at week 12. (A) *The IVIS® Spectrum in vivo imaging of the calvaria shows the presence of the red-fluorescent exogenous mTmG MSC in all conditions, confirming the engraftment of the supplied MSC. The intensity of the fluorescence shows the concentration of cells in the defect area. (B) Confocal fluorescent image of the OD-MSC construct with fibrin carrier gel show the presence of red-fluorescent mTmG MSC. The cells were counterstained with DAPI nuclear stain.*

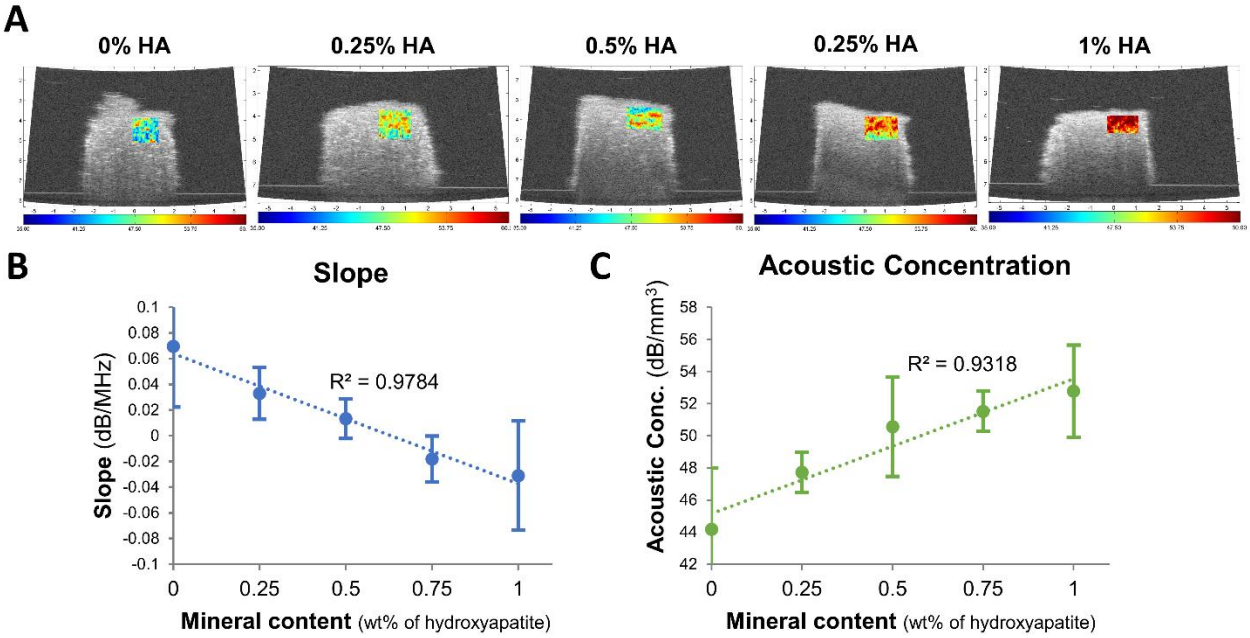

Supplementary Figure 6 The spectral ultrasound imaging (SUSI) to quantify the mineral content of the implanted tissues. *(A) The Grayscale images of the constructs made up of microtissue with 0.0 to 1.0% HA overlaid with the corresponding acoustic concentration values show an upward trend. (B) A plot of the mineral content of the microtissues versus the slope of the plot showed substantial agreement (R=0.97). (C) A plot of the mineral content of the microtissues versus the acoustic concentration showed substantial agreement (R=0.93)*

Reference:

1. Dimitriou, R., et al., *Complications following autologous bone graft harvesting from the iliac crest and using the RIA: A systematic review.* Injury, 2011. **42**(Supplement 2): p. S3-S15.

2. Arrington, E.D., et al., *Complications of iliac crest bone graft harvesting.* Clin Orthop Relat Res, 1996(329): p. 300-9.

3. Janicki, P. and G. Schmidmaier, *What should be the characteristics of the ideal bone graft substitute? Combining scaffolds with growth factors and/or stem cells.* Injury, 2011. **42**(Supplement 2): p. S77-S81.

4. Wang, S., et al., *Maintenance of phenotype and function of cryopreserved bone-derived cells.* Biomaterials, 2011. **32**(15): p. 3739-49.

5. Bianco, P. and P.G. Robey, *Stem cells in tissue engineering.* Nature, 2001. **414**(6859): p. 118-21.

6. Chatterjea, A., et al., *Clinical Application of Human Mesenchymal Stromal Cells for Bone Tissue Engineering.* Stem Cells International, 2010. **2010**: p. 12.

7. Chang, B., et al., *Injectable scaffolds: Preparation and application in dental and craniofacial regeneration.* Mater Sci Eng R Rep, 2017. **111**: p. 1-26.

8. Dreifke, M.B., N.A. Ebraheim, and A.C. Jayasuriya, *Investigation of potential injectable polymeric biomaterials for bone regeneration.* Journal of biomedical materials research. Part A, 2013. **101**(8): p. 2436-2447.

9. Barrère, F., et al., *Advanced biomaterials for skeletal tissue regeneration: Instructive and smart functions.* Materials Science and Engineering: R: Reports, 2008. **59**(1): p. 38-71.

10. Shoulders, M.D. and R.T. Raines, *Collagen Structure and Stability.* Annual Review of Biochemistry, 2009. **78**(1): p. 929-958.

11. Chicatun, F., et al., *8 - Collagen/chitosan composite scaffolds for bone and cartilage tissue engineering A2 - Ambrosio, Luigi*, in *Biomedical Composites (Second Edition)*. 2017, Woodhead Publishing. p. 163-198.

12. Du, C., et al., *Formation of calcium phosphate/collagen composites through mineralization of collagen matrix.* Journal of Biomedical Materials Research, 2000. **50**(4): p. 518-527.

13. Dubey, D.K. and V. Tomar, *Role of the nanoscale interfacial arrangement in mechanical strength of tropocollagen–hydroxyapatite-based hard biomaterials.* Acta Biomaterialia, 2009. **5**(7): p. 2704-2716.

14. Venkatesan, J. and S.K. Kim, *Chitosan composites for bone tissue engineering--an overview.* Mar Drugs, 2010. **8**(8): p. 2252-66.

15. Wang, L. and J.P. Stegemann, *Glyoxal crosslinking of cell-seeded chitosan/collagen hydrogels for bone regeneration.* Acta Biomater, 2011. **7**(6): p. 2410-7.

16. Wise, J.K., et al., *Synergistic enhancement of ectopic bone formation by supplementation of freshly isolated marrow cells with purified MSC in collagen-chitosan hydrogel microbeads.* Connect Tissue Res, 2016. **57**(6): p. 516-525.

17. Levi, B., et al., *Human adipose derived stromal cells heal critical size mouse calvarial defects.* PLoS One, 2010. **5**(6): p. e11177.

18. C.E., M., *Density of Bone: Effects on surgical approach and healing*, in *Contemporary Implant Dentistry*, C.E. Misch, Editor. 2008, Elsevier: Canada. p. 645-667.

19. Clayden, N. and R. Williams, *Peptide group shifts.* Journal of Magnetic Resonance (1969), 1982. **49**(3): p. 383-396.

20. Agarwal, S., et al., *Inhibition of Hif1alpha prevents both trauma-induced and genetic heterotopic ossification.* Proc Natl Acad Sci U S A, 2016. **113**(3): p. E338-47.

21. Peterson, J.R., et al., *Burn injury enhances bone formation in heterotopic ossification model.* Ann Surg, 2014. **259**(5): p. 993-8.

22. Ranganathan, K., et al., *Role of gender in burn-induced heterotopic ossification and mesenchymal cell osteogenic differentiation.* Plast Reconstr Surg, 2015. **135**(6): p. 1631-41.

23. Nor, J.E., et al., *Engineering and Characterization of Functional Human Microvessels in Immunodeficient Mice.* Lab Invest, 2001. **81**(4): p. 453-463.

24. Gudur, M.S.R., et al., *Noninvasive Quantification of In Vitro Osteoblastic Differentiation in 3D Engineered Tissue Constructs Using Spectral Ultrasound Imaging.* Plos One, 2014. **9**(1).

25. Kneser, U., et al., *Tissue engineering of bone: the reconstructive surgeon's point of view.* Journal of Cellular and Molecular Medicine, 2006. **10**(1): p. 7-19.

26. Logeart-Avramoglou, D., et al., *Engineering bone: challenges and obstacles.* Journal of Cellular and Molecular Medicine, 2005. **9**(1): p. 72-84.

27. Mitchell, J.B., et al., *Immunophenotype of Human Adipose-Derived Cells: Temporal Changes in Stromal-Associated and Stem Cell–Associated Markers.* STEM CELLS, 2006. **24**(2): p. 376-385.

28. Huang, J.I., et al., *Chondrogenic potential of multipotential cells from human adipose tissue.* Plast Reconstr Surg, 2004. **113**(2): p. 585-94.

29. Gimble, J.M., A.J. Katz, and B.A. Bunnell, *Adipose-Derived Stem Cells for Regenerative Medicine.* Circulation Research, 2007. **100**(9): p. 1249-1260.

30. Gimble, J.M., et al., *Adipose-derived stromal/stem cells: A primer.* Organogenesis, 2013. **9**(1): p. 3-10.

31. Mizuno, H., et al., *Myogenic differentiation by human processed lipoaspirate cells.* Plastic and Reconstructive Surgery, 2002. **109**(1): p. 199-209.

32. Xu, Y., et al., *Adipose-derived mesenchymal cells as a potential cell source for skeletal regeneration.* Current Opinion in Molecular Therapeutics, 2005. **7**(4): p. 300-305.

33. Anna, B., et al., *Encapsulation of adult human mesenchymal stem cells within collagen-agarose microenvironments.* Biotechnology and Bioengineering, 2005. **92**(4): p. 492-500.

34. Gao, F., et al., *Mesenchymal stem cells and immunomodulation: current status and future prospects.* Cell Death & Disease, 2016. **7**(1): p. e2062.

35. Gronthos, S., et al., *Surface protein characterization of human adipose tissue-derived stromal cells.* Journal of Cellular Physiology, 2001. **189**(1): p. 54-63.

36. Cui, L., et al., *Expanded adipose-derived stem cells suppress mixed lymphocyte reaction by secretion of prostaglandin E2.* Tissue Engineering, 2007. **13**(6): p. 1185-1195.

37. Qiu, G., et al., *Adipose-derived mesenchymal stem cells modulate CD14(++)CD16(+) expression on monocytes from sepsis patients in vitro via prostaglandin E2.* Stem Cell Research & Therapy, 2017. **8**: p. 97.

38. Németh, K., et al., *Bone marrow stromal cells attenuate sepsis via prostaglandin E2–dependent reprogramming of host macrophages to increase their interleukin-10 production.* Nature Medicine, 2008. **15**: p. 42.

39. Liu, Q.H., et al., *The Role of the Extracellular Signal-Related Kinase Signaling Pathway in Osteogenic Differentiation of Human Adipose-Derived Stem Cells and in Adipogenic Transition Initiated by Dexamethasone.* Tissue Engineering Part A, 2009. **15**(11): p. 3487-3497.

40. Cho, H.H., et al., *NF-κB activation stimulates osteogenic differentiation of mesenchymal stem cells derived from human adipose tissue by increasing TAZ expression.* Journal of Cellular Physiology, 2010. **223**(1): p. 168-177.

41. Guihard, P., et al., *Induction of Osteogenesis in Mesenchymal Stem Cells by Activated Monocytes/Macrophages Depends on Oncostatin M Signaling.* STEM CELLS, 2012. **30**(4): p. 762-772.

42. Thesleff, T., et al., *Cranioplasty with Adipose-Derived Stem Cells, Beta-Tricalcium Phosphate Granules and Supporting Mesh: Six-Year Clinical Follow-Up Results.* Stem Cells Transl Med, 2017. **6**(7): p. 1576-1582.

43. Tiruvannamalai-Annamalai, R., D.R. Armant, and H.W.T. Matthew, *A Glycosaminoglycan Based, Modular Tissue Scaffold System for Rapid Assembly of Perfusable, High Cell Density, Engineered Tissues.* PLOS ONE, 2014. **9**(1): p. e84287.

44. Sándor, G.K., et al., *Adipose Stem Cell Tissue–Engineered Construct Used to Treat Large Anterior Mandibular Defect: A Case Report and Review of the Clinical Application of Good Manufacturing Practice–Level Adipose Stem Cells for Bone Regeneration.* Journal of Oral and Maxillofacial Surgery, 2013. **71**(5): p. 938-950.

45. Lu, Z., et al., *Priming Adipose Stem Cells with Tumor Necrosis Factor-Alpha Preconditioning Potentiates Their Exosome Efficacy for Bone Regeneration.* Tissue Engineering Part A, 2017. **23**(21-22): p. 1212-1220.

46. Behnia, H., et al., *Repair of alveolar cleft defect with mesenchymal stem cells and platelet derived growth factors: A preliminary report.* Journal of Cranio-Maxillofacial Surgery, 2012. **40**(1): p. 2-7.

47. Zhou, Y., et al., *Mesenchymal stromal cells regulate the cell mobility and the immune response during osteogenesis through secretion of vascular endothelial growth factor A.* Journal of Tissue Engineering and Regenerative Medicine, 2017: p. n/a-n/a.

48. Langenbach, F. and J. Handschel, *Effects of dexamethasone, ascorbic acid and beta-glycerophosphate on the osteogenic differentiation of stem cells in vitro.* Stem Cell Res Ther, 2013. **4**(5): p. 117.

49. Yu, S.P., Z. Wei, and L. Wei, *Preconditioning strategy in stem cell transplantation therapy.* Transl Stroke Res, 2013. **4**(1): p. 76-88.

50. Valorani, M.G., et al., *Pre-culturing human adipose tissue mesenchymal stem cells under hypoxia increases their adipogenic and osteogenic differentiation potentials.* Cell Proliferation, 2012. **45**(3): p. 225-238.

51. Han, Y.-S., et al., *Hypoxia-induced expression of cellular prion protein improves the therapeutic potential of mesenchymal stem cells.* Cell Death &Amp; Disease, 2016. **7**: p. e2395.

52. Greijer, A.E. and E. van der Wall, *The role of hypoxia inducible factor 1 (HIF-1) in hypoxia induced apoptosis.* Journal of Clinical Pathology, 2004. **57**(10): p. 1009-1014.

53. Tiruvannamalai Annamalai, R., et al., *Vascular Network Formation by Human Microvascular Endothelial Cells in Modular Fibrin Microtissues.* ACS Biomaterials Science & Engineering, 2016. **2**(11): p. 1914-1925.

54. Rioja, A.Y., et al., *Endothelial sprouting and network formation in collagen- and fibrin-based modular microbeads.* Acta Biomaterialia, 2016. **29**: p. 33-41.

55. Murphy, K.C., S.Y. Fang, and J.K. Leach, *Human mesenchymal stem cell spheroids in fibrin hydrogels exhibit improved cell survival and potential for bone healing.* Cell and Tissue Research, 2014. **357**(1): p. 91-99.

56. Rao, R.R., et al., *Dual-phase osteogenic and vasculogenic engineered tissue for bone formation.* Tissue Eng Part A, 2015. **21**(3-4): p. 530-40.

57. Gudur, M., et al., *Noninvasive, quantitative, spatiotemporal characterization of mineralization in three-dimensional collagen hydrogels using high-resolution spectral ultrasound imaging.* Tissue Eng Part C Methods, 2012. **18**(12): p. 935-46.